

Compact Multi-level-prior Tensor Representation for Hyperspectral Image Super-resolution

Yinjian Wang, Wei Li, *Senior Member, IEEE*, Yuanyuan Gui, Gemine Vivone, *Senior Member, IEEE*

Abstract—Fusing a hyperspectral image with a multispectral image acquired over the same scene, *i.e.*, hyperspectral image super-resolution, has become a popular computational way to access the latent high-spatial-spectral-resolution image. To date, a variety of fusion methods have been proposed, among which the tensor-based ones have testified that multiple priors, such as multidimensional low-rankness and spatial total variation at multiple levels, effectively drive the fusion process. However, existing tensor-based models can only effectively leverage one or two priors at one or two levels, since simultaneously incorporating multi-level priors inevitably increases model complexity. This introduces challenges in both balancing the weights of different priors and optimizing multi-block structures. Concerning this, we present a novel hyperspectral super-resolution model compactly characterizing these multi-level priors of hyperspectral images within the tensor framework. Firstly, the proposed model decouples the spectral low-rankness and spatial priors by casting the latent high-spatial-spectral-resolution image into spectral subspace and spatial maps via block term decomposition. Secondly, these spatial maps are stacked as the spatial tensor encoding the high-order spatial low-rankness and smoothness priors, which are co-modeled via the proposed non-convex mode-shuffled tensor correlated total variation. Finally, we draw inspiration from the linearized alternating direction method of multipliers to design an efficient algorithm to optimize the resulting model, theoretically proving its Karush-Kuhn-Tucker convergence under mild conditions. Experiments on multiple datasets demonstrate the effectiveness of the proposed algorithm. The code implementation will be available from <https://github.com/WongYinJ>.

Index Terms—Low-rank tensor, total variation, non-convex optimization, hyperspectral super-resolution, image fusion, remote sensing.

I. INTRODUCTION

Hyperspectral image (HSI) is much appreciated for its nanometer-level fine-grained spectral information which to a large extent facilitates many scene interpretation tasks such as classification [1], [2], object tracking [3], and target detection [4], [5]. Unfortunately, acquiring high-spatial-resolution HSI at the hardware level remains a significant challenge due to the fundamental physical trade-offs in existing imaging systems. To be more specific, the desire for adequate photon capture to maintain photoelectric signal-to-noise-ratio necessitates larger

detector units per spectral band in hyperspectral sensors, inherently reducing the spatial resolution of the acquired HSI. Such defect severely impairs the delineation of fine-scale features in the application scenarios above [6]. Consequently, fusing HSI with a corresponding multi-spectral image (MSI) that is easily captured at a much higher spatial resolution due to a much sparser spectral sampling rate [7], *i.e.*, hyperspectral super-resolution (HSR), has become a popular software-level alternative to access to the latent high-spatial-spectral-resolution image (HSSI).

In this vein, numerous HSR models have been subsequently proposed. Song *et al.* [8] developed a dictionary-based fusion method using non-negative matrix factorization to couple spectral and spatial information from HSI and MSI, respectively, achieving higher-fidelity results than benchmarks on satellite data. A convex alternating direction method of multipliers (ADMM)-based fusion method that leverages subspace modeling and edge-preserving vector total variation (TV) regularization to achieve HSR has been presented in [9], which jointly estimates the spatial and spectral responses that degrade the latent HSSI. Wei *et al.* [10] modeled HSR as the problem of solving a Sylvester equation maximizing the likelihood criterion. By leveraging the structural properties of the circulant and downsampling matrices inherent to the fusion problem, they derived a closed-form solution for the associated Sylvester equation, eliminating the need for iterative updates. Dian *et al.* [11] framed the fusion task as estimating spectral basis functions and their corresponding coefficients, and integrated non-local spatial similarities, spectral unmixing priors, and a sparsity constraint into the fusion problem. Xue *et al.* [12] proposed a structured sparse low-rank representation model that effectively exploits spatial/spectral subspace relationships from higher-level analysis, achieving superior HSR performance.

Despite their promising performance, all those methods fail to outrun the regime of matricizing the 3D HSI data cube. Since matrix analysis relies on the conventional matrix product, which only captures row-column relationships, it struggles to model the intricate structures of high-dimensional data like HSI. Consequently, tensor-based HSR approaches have gained increasing attention in HSI analysis [13]. Exploiting a coupled Tucker decomposition [14] paradigm, Dian *et al.* [15] translated the spatial-spectral correlation of HSSI into the sparse prior on the core tensor and delivered a coupled sparse tensor factorization (CSTF) HSR model, which was later generalized for semi-blind HSR [16]. Chang *et al.* [17] proposed a HSI restoration model that simultaneously captures spectral-spatial nonlocal similarity and spectral correlation

This paper was supported by NSFC Projects of International Cooperation and Exchanges [Grant number W2411055]. (Corresponding author: Wei Li.)

Y. Wang, W. Li, and Y. Gui are with the School of Information and Electronics, Beijing Institute of Technology, and the National Key Laboratory of Science and Technology on Space-Born Intelligent Information Processing, Beijing 100081, China (e-mail: yinwj@bit.edu.cn, liwei089@ieee.org, 953647315@qq.com).

G. Vivone is with the National Research Council, Institute of Methodologies for Environmental Analysis (CNR-IMAA), 85050 Tito, Italy (e-mail: gemine.vivone@imaa.cnr.it).

through third-order tensors, demonstrating how singular value reweighting significantly enhances tensor modeling capability and flexibility. As research progresses, it is acknowledged that HSI exhibits multi-dimensional structures that cannot be sufficiently characterized by imposing a single constraint on any individual factor. In light of this, Dian *et al.* [18] exploited the low tensor-train (TT) [19] rank (LTTR) prior, formulated in a multi-rank form, of the grouped 4D non-local patch tensors. They also proposed the generalized tensor nuclear norm (GTNN) [20] to promote flexibility when characterizing the multi-dimensional low tensor tubal rank [21]. To avoid the computational burden inherited from patch clustering, Liu *et al.* [22] imposed the tensor trace norm [23] straightforwardly on the HSSI to cast the HSR task as a low Tucker rank tensor approximation (LRTA) problem. However, these methods formulate the multi-dimensional rank minimization problem as minimizing the nuclear norms of several matrices unfolded from the desired HSSI, incapable of explicitly analyzing the structures of the decomposed factors [24]. To overcome this limitation, Li *et al.* [25] proposed the anisotropic sparsity (AS) tensor norm to transform the multi-dimensional low-rankness of the original tensor into the multi-dimensional sparsity of the Tucker core tensor. The resulting AS constrained low-rank tensor approximation (ASLA) framework achieves simultaneous multi-dimensional prior exploitation and factor structure pursuit under Tucker decomposition. Xu *et al.* [26] proposed the cascade-transform based tensor nuclear norm to alleviate the boundary effects and singleton domain limitation accompanied with the conventional tensor nuclear norm (TNN), which, noteworthy, was then generalized into a full-scale/multi-dimensional version, reducing its directional sensitivity. Another variant of TNN based on a non-linear transform, along with its full-scale/multi-dimensional version, was presented in [27], breaking TNN's limitation in modeling complex data structures inherent in the linear transform. Additionally, TV [28], as an efficient tool modeling the spatial continuity equipped within diverse image modalities, has been successfully absorbed into tensor-based HSR frameworks, *e.g.*, [25], [29], [30], [31], [32]. However, with multi-prior being employed, these models inevitably increase by scale, which leads to the challenges of model selection and multi-block optimization. Thus many of them suffer from hyper-weight balancing and the loss of convergence guarantee. Besides, most of these methods only manage to extract those prior information from a single level, that is, from the original data or its factorized components. The comprehensive exploitation of multi-prior at multi-level remains an open issue.

The advancement of computing devices has enabled the development of deep learning techniques. The HSR field has therefore witnessed a proliferation of data-driven methods. Nguyen *et al.* [33] proposed an unsupervised CNN-based fusion framework that incorporates Stein's unbiased risk estimate (SURE) into a novel loss function, combining backprojection mean square error (MSE) with SURE to approximate the projected MSE between the fused and ground-truth HSSIs. Inspired by the smoothed particle hydrodynamics (SPH) theory, [34] analogized pixel motion to SPH particle dynamics, implementing multi-scale smooth convolutions to preserve

spectral information while using discretized Navier-Stokes equations to guide pixel motion for enhanced spatial edge clarity. Dian *et al.* [35] delivered a zero-shot learning (ZSL) HSR network that estimates sensor responses for realistic data simulation, also incorporating dimension reduction and model-based loss, thus overcoming data scarcity/generalization issues while maintaining high accuracy and efficiency. Ma *et al.* [36] replaced convolutional neural network (CNN) with transformers to learn HSSI priors, and unfolded a proximal gradient algorithm into a network where self-attention captures global spatial interactions and 3D-CNN layers enhance spatial-spectral correlation modeling. Nevertheless, the reliance on large-scale computational resources and high-quality training data remains a critical limitation hindering the practical application of data-driven methods.

In such context, this paper presents an as compact as possible tensor model for the HSR task, to concisely realize multi-level-prior representation, which further facilitates a convergence-guaranteed iterative algorithm. Specifically, the contributions are three-folds:

(1) We present the non-convex mode-shuffled tensor correlated total variation (NMS-t-CTV), which modifies t-CTV [37] with a designed mode-shuffle strategy improving from convex approximation to non-convex one. By imposing it on the stacked spatial tensor acquired from the block-term decomposition (BTD) [38], we theoretically justify that the resulting model can cross-represent multi-level-priors equipped within the latent HSSI in a compact form.

(2) Inspired by the linearized alternating direction method of multipliers (LADMM) [39], [40], we customize an optimization framework for the proposed model that successfully deals with the high dimensionality of the spatial tensor. With a mild assumption that some multipliers are bounded, we manage to theoretically guarantee the convergence of the optimization framework to the Karush-Kuhn-Tucker (KKT) [41], [42], [43] point, which also benefits from the compactness of the proposed model.

(3) A broad experimental analysis demonstrates the practical efficacy of the proposed compact multi-level-prior tensor representation (CMIpTR).

The remainder of this article is organized as follows. Sec. II familiarizes the readers with the notation and the foundational concepts related to this paper. Sec. III presents the proposed CMIpTR and the derivation of the optimization framework. Sec. IV shows the experimental results. Finally, Sec. V draws the conclusions.

II. PREPARATION

A. Notations

Throughout this article, we denote a scalar as a , a vector as \mathbf{a} , a matrix as \mathbf{A} , and a tensor as \mathcal{A} . $\|\mathbf{A}\|_F$, $\|\mathbf{A}\|$, $\|\mathbf{A}\|_1$, and $\|\mathbf{A}\|_*$ denote the Frobenius, the l_1 , and the nuclear norms of a matrix, respectively. Particularly, we use \mathbf{I}_N to denote the $N \times N$ identity matrix, \mathbf{F}_N to denote the $N \times N$ discrete Fourier transformation matrix, and \mathbf{D}_N to denote the $(N -$

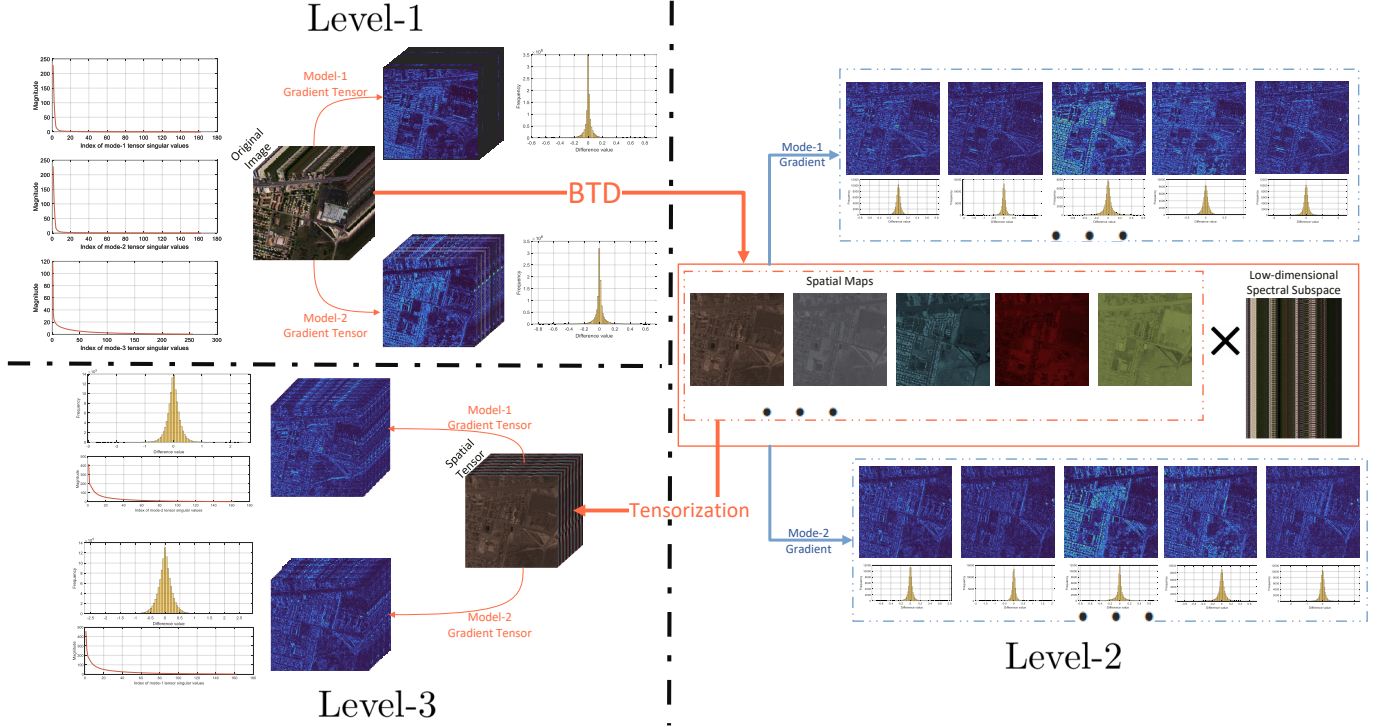


Fig. 1: Multi-level-prior observation. Level-1: the original data domain; level-2: the factorization domain; Level-3: the enhanced tensorization domain.

\mathcal{S} , while the spatial smoothness is encoded in the horizontal and vertical gradients of the spatial maps.

Moreover, [49] has suggested that by inspecting the stacked spatial tensor \mathcal{A} instead of the spatial maps, we get the enhanced version of spatial priors. To this end, and also inspired by t-CTV, we examine the spatial TV and low-rankness both from the gradient tensors of \mathcal{A} , as visualized by the Level-3 part of Fig. 1.

Thus, taking $\mathcal{Z} = \mathcal{A} \times_3 \mathcal{S}$ into Eq. (II-C.1), the HSR problem is reformulated as:

$$\text{Find } \mathcal{A}, \mathcal{S}, \quad \text{s.t.}, \quad \mathcal{X} = \mathcal{A} \times_1 \mathbf{P}_1 \times_2 \mathbf{P}_2 \times_3 \mathcal{S}, \\ \mathcal{Y} = \mathcal{A} \times_3 \mathbf{P}_3 \mathcal{S}.$$

B. Multi-level-prior Tensor Representation

As it is observed that multi-level-priors are equipped within the HSSI in the BTD paradigm, we now establish a constraint to compactly represent these multi-level-priors. While t-CTV jointly enforces low-rankness and smoothness via a nuclear norm constraint on gradient tensors, it computes the norm uniformly across all modes. This fixed-mode pattern lacks the flexibility to capture the distinct structural priors along different dimensions of HSSI data. To address this limitation, we propose NMS-t-CTV, which adaptively imposes mode-specific low-rank constraints on gradient tensors for more accurate prior characterization.

Definition III-B.1 (NMS-t-CTV): For the spatial tensor \mathcal{A} defined in Eq. (III-A.1), its NMS-t-CTV, denoted as $\|\mathcal{A}\|_{*,\psi}$,

is defined as:

$$\|\mathcal{A}\|_{*,\psi} = \frac{1}{2} \sum_{n=1}^2 \|\mathcal{A} \times_n \mathbf{D}_{I_n}\|_{3-n, \psi}$$

In the definition above, the mode along which the LTSVDR is employed with respect to each gradient tensor is designed. Specifically, for the mode-1 gradient tensor, its mode-2 LTSVDR is considered while the mode-1 LTSVDR is imposed on the mode-2 gradient tensor. This facilitates the cross-representation of multi-level-priors in a compact way. Besides, we employ the NTPNN in replacement of the convex TNN to achieve tighter approximation of the tensor rank. By doing so, the proposed CMlpTR model for HSR is as follows:

$$\min_{\mathcal{A}, \mathcal{S}} \frac{1}{2} \sum_{n=1}^2 \|\mathcal{A} \times_n \mathbf{D}_{I_n}\|_{3-n, \psi}, \\ \text{s.t.}, \quad \mathcal{X} = \mathcal{A} \times_1 \mathbf{P}_1 \times_2 \mathbf{P}_2 \times_3 \mathcal{S}, \\ \mathcal{Y} = \mathcal{A} \times_3 \mathbf{P}_3 \mathcal{S}. \quad (\text{III-B.1})$$

Model (III-B.1) is then designed to compactly co-represent the aforementioned multi-level-priors with only two-block variables and two constraints. To help justifying its ability, we deliver Prop. III-B.1 below.

Proposition III-B.1: Regarding Eq. (III-A.1), if $\mathcal{S} \in \mathbb{R}^{I_3 \times R}$ is semi-unitary, i.e., $\mathcal{S}^* \mathcal{S} = \mathbf{I}_R$, there follows:

$$\text{rank}_{3-n}^t(\mathcal{Z}) - 1 \leq \text{rank}_{3-n}^t(\mathcal{A} \times_n \mathbf{D}_{I_n}) \leq \text{rank}_{3-n}^t(\mathcal{Z}), \\ n = 1, 2. \quad (\text{III-B.2})$$

If we further have that \mathcal{A} is bounded and $\psi(\cdot)$ is endowed with the properties that:

P1: $\psi(\cdot)$ is concave and non-decreasing, with $\psi(0) = 0$,

P2: $\psi'(\cdot)$ is convex and non-increasing, with $\lim_{x \rightarrow 0^+} \psi'(x) < \infty$,

then the NMS-t-CTV is compatible with the TV norms, *i.e.*, $\exists a_1, a_2, a_3, a_4 > 0$, such that

$$\begin{aligned} a_1 \|\mathcal{A}\|_{TV} &\leq \|\mathcal{A}\|_{\tilde{*}, \psi} \leq a_2 \|\mathcal{A}\|_{TV}, \\ a_3 \|\mathcal{A}\|_{ATV} &\leq \|\mathcal{A}\|_{\tilde{*}, \psi} \leq a_4 \|\mathcal{A}\|_{ATV}. \end{aligned} \quad (\text{III-B.3})$$

Proof: Deferred to Sec. I in Appendix. ■

As a result, the co-representation ability of our CMlpTR can be explained as follows.

(1) Since \mathcal{S} encodes the spectral subspace of HSI/HSSI, the spectral low-rankness of \mathcal{Z} can be modeled by controlling the dimensionality of \mathcal{S} .

(2) According to Remark 1 in [37], the multi-dimensional mode- $\{1,2\}$ LTR of \mathcal{A} is well captured.

(3) Based on Eq. (III-B.2), our CMlpTR can express the spatial low-rankness of the original \mathcal{Z} , which together with (1) realizes the co-representation of the multi-dimensional LTR within \mathcal{Z} .

(4) Eq. (III-B.3) asserts that the spatial TV prior of HSI/HSSI, reflected on the spatial tensor \mathcal{A} , is well characterized. Moreover, since we have $\|\mathcal{A}\|_{ATV} = \sum_{r=1}^R \|\mathcal{A}_{::,r}\|_{ATV}$, the TV prior on the 2D spatial maps of the BTD level is also expressed.

Besides, it is known from Prop. III-B.1 that to take (1)-(4) into effect, some additional conditions should be satisfied by \mathcal{S} and $\psi(\cdot)$. Thus, we specify the non-convex surrogate as $\psi(x) = \frac{\log(\gamma x + 1)}{\log(\gamma + 1)}$ [50] and add the semi-unitary constraint on \mathcal{S} to obtain:

$$\begin{aligned} \min_{\mathcal{A}, \mathcal{S}} \quad & \frac{1}{2} \sum_{n=1}^2 \|\mathcal{A} \times_n \mathbf{D}_{I_n}\|_{\tilde{*}, \psi}^{3-n}, \\ \text{s.t.}, \quad & \mathcal{X} = \mathcal{A} \times_1 \mathbf{P}_1 \times_2 \mathbf{P}_2 \times_3 \mathcal{S}, \\ & \mathcal{Y} = \mathcal{A} \times_3 \mathbf{P}_3 \mathcal{S}, \\ & \mathbf{S}^* \mathbf{S} = \mathbf{I}_R. \end{aligned} \quad (\text{III-B.4})$$

C. Optimization Algorithm

To find a solution to Problem (III-B.4), it is noticed that auxiliary variables are unavoidable in solving the \mathcal{A} -subproblems, leading to the expansion of the problem scale. In [48], the authors demonstrate that the subspace and coefficient can be determined in a sequential manner without hurting the model performance. Thus, we extract the semi-unitary spectral subspace \mathcal{S} simply from HSI \mathcal{X} as:

$$[\mathcal{S}, \sim, \sim] = \text{svds}(\mathcal{X}_{[3]}, R).$$

Then, the problem can be reduced as:

$$\begin{aligned} \min_{\mathcal{A}} \quad & \frac{1}{2} \sum_{n=1}^2 \|\mathcal{A} \times_n \mathbf{D}_{I_n}\|_{\tilde{*}, \psi}^{3-n}, \\ \text{s.t.}, \quad & \mathcal{X} = \mathcal{A} \times_1 \mathbf{P}_1 \times_2 \mathbf{P}_2 \times_3 \mathcal{S}, \\ & \mathcal{Y} = \mathcal{A} \times_3 \mathbf{P}_3 \mathcal{S}, \end{aligned}$$

to solve it, we introduce some auxiliary variables, *i.e.*, \mathcal{G}_1 and \mathcal{G}_2 , and we obtain:

$$\begin{aligned} \min_{\mathcal{A}, \{\mathcal{G}_n\}_{n=1,2}} \quad & \frac{1}{2} \sum_{n=1}^2 \|\mathcal{G}_n\|_{\tilde{*}, \psi}^{3-n}, \\ \text{s.t.}, \quad & \mathcal{X} = \mathcal{A} \times_1 \mathbf{P}_1 \times_2 \mathbf{P}_2 \times_3 \mathcal{S}, \\ & \mathcal{Y} = \mathcal{A} \times_3 \mathbf{P}_3 \mathcal{S}, \\ & \mathcal{G}_n = \mathcal{A} \times_n \mathbf{D}_{I_n}, n = 1, 2. \end{aligned} \quad (\text{III-C.1})$$

Usually, problem like (III-C.1) is easily solved by ADMM [51]. However, the \mathcal{A} -subproblem suffers from the high-dimensionality of \mathcal{A} , compelling us to make adjustment to its ADMM-induced updating steps. The resulting algorithm can be viewed as a composition of LADMM. Below, we elaborate on it and provide its convergence analysis in Thm. III-D.1.

Let us start defining the augmented Lagrangian function of (III-C.1) as:

$$\begin{aligned} L(\mathcal{A}, \{\mathcal{G}_n\}_{n=1,2}, \mathcal{M}_x, \mathcal{M}_y, \{\mathcal{M}_n\}_{n=1,2}) \\ = \frac{1}{2} \sum_{n=1}^2 \|\mathcal{G}_n\|_{\tilde{*}, \psi}^{3-n} + \frac{\rho}{2} \left(\left\| \mathcal{X} + \frac{\mathcal{M}_x}{\rho} - \mathcal{A} \times_1 \mathbf{P}_1 \times_2 \right. \right. \\ \left. \left. \mathbf{P}_2 \times_3 \mathcal{S} \right\|_F^2 + \left\| \mathcal{Y} + \frac{\mathcal{M}_y}{\rho} - \mathcal{A} \times_3 \mathbf{P}_3 \mathcal{S} \right\|_F^2 \right. \\ \left. + \sum_{n=1}^2 \left\| \mathcal{G}_n + \frac{\mathcal{M}_n}{\rho} - \mathcal{A} \times_n \mathbf{D}_{I_n} \right\|_F^2 \right) \\ - \frac{1}{2\rho} \left(\left\| \mathcal{M}_x \right\|_F^2 + \left\| \mathcal{M}_y \right\|_F^2 + \sum_{n=1}^2 \left\| \mathcal{M}_n \right\|_F^2 \right) \end{aligned} \quad (\text{III-C.2})$$

where $\{\mathcal{M}_x, \mathcal{M}_y, \{\mathcal{M}_n\}_{n=1,2}\}$ are the Lagrangian multipliers and ρ is the penalty parameter.

- \mathcal{A} -subproblem: Fixing $\{\mathcal{G}_n\}_{n=1,2}$, \mathcal{A} is updated via solving

$$\begin{aligned} \min_{\mathcal{A}} L_1(\mathcal{A}) \triangleq & \left\| \mathcal{X} + \frac{\mathcal{M}_x}{\rho} - \mathcal{A} \times_1 \mathbf{P}_1 \times_2 \mathbf{P}_2 \times_3 \mathcal{S} \right\|_F^2 \\ & + \left\| \mathcal{Y} + \frac{\mathcal{M}_y}{\rho} - \mathcal{A} \times_3 \mathbf{P}_3 \mathcal{S} \right\|_F^2 \\ & + \sum_{n=1}^2 \left\| \mathcal{G}_n + \frac{\mathcal{M}_n}{\rho} - \mathcal{A} \times_n \mathbf{D}_{I_n} \right\|_F^2. \end{aligned} \quad (\text{III-C.3})$$

Typically, Eq. (III-C.3) can be easily solved by setting its gradient to zero. However, the high-dimensionality of \mathcal{A} is a curse for doing so. Thus, inspired by LADMM, we approximate its solution by a simple one-step gradient descend, *i.e.*

$$\mathcal{A} \leftarrow \mathcal{A} - \frac{\nabla L_1(\mathcal{A})}{\tau} \quad (\text{III-C.4})$$

in which the gradient is calculated as

$$\begin{aligned} & \nabla L_1(\mathcal{A}) \\ = & 2 \left(\mathcal{A} \times_1 \mathbf{P}_1^* \mathbf{P}_1 \times_2 \mathbf{P}_2^* \mathbf{P}_2 + \mathcal{A} \times_3 \mathbf{S}^* \mathbf{P}_3^* \mathbf{P}_3 \mathbf{S} \right. \\ & + \sum_{n=1}^2 \mathcal{A} \times_n \mathbf{D}_{I_n}^* \mathbf{D}_{I_n} - \left(\mathcal{X} + \frac{\mathcal{M}_x}{\rho} \right) \times_1 \mathbf{P}_1^* \times_2 \mathbf{P}_2^* \\ & \times_3 \mathbf{S}^* - \left(\mathcal{Y} + \frac{\mathcal{M}_y}{\rho} \right) \times_3 \mathbf{S}^* \mathbf{P}_3^* - \\ & \left. \sum_{n=1}^2 \left(\mathcal{G}_n + \frac{\mathcal{M}_n}{\rho} \right) \times_n \mathbf{D}_{I_n}^* \right) \end{aligned} \quad (\text{III-C.5})$$

and the updating stride τ should satisfy the Lipschitz continuity condition that

$$\left\| \nabla L_1(\mathcal{A}) - \nabla L_1(\mathcal{A}') \right\|_F \leq \tau \left\| \mathcal{A} - \mathcal{A}' \right\|_F \quad (\text{III-C.6})$$

for any $\mathcal{A}, \mathcal{A}'$. To this end, we set

$$\tau = 2 \left(\left\| \mathbf{P}_1 \right\|^2 \left\| \mathbf{P}_2 \right\|^2 + \left\| \mathbf{P}_3 \mathbf{S} \right\|^2 + \left\| \mathbf{P}_1 \right\|^2 + \left\| \mathbf{P}_2 \right\|^2 \right). \quad (\text{III-C.7})$$

- \mathcal{G}_n -subproblem, $n = 1, 2$: Fixing \mathcal{A} , \mathcal{G}_n is updated by solving

$$\begin{aligned} \min_{\mathcal{G}_n} L_{n+1}(\mathcal{G}_n) \triangleq & \left\| \mathcal{G}_n \right\|_{*,\psi}^{3-n} \\ & + \rho \left\| \mathcal{G}_n + \frac{\mathcal{M}_n}{\rho} - \mathcal{A} \times_n \mathbf{D}_{I_n} \right\|_F^2 \end{aligned} \quad (\text{III-C.8})$$

which is equivalent to

$$\begin{aligned} \min_{\mathcal{G}_n} L_{n+1}(\mathcal{G}_n) \triangleq & \left\| \mathbf{P}_{3-n}(\mathcal{G}_n) \right\|_{*,\psi}^n \\ & + \rho \left\| \mathbf{P}_{3-n}(\mathcal{G}_n) + \mathbf{P}_{3-n} \left(\frac{\mathcal{M}_n}{\rho} - \mathcal{A} \times_n \mathbf{D}_{I_n} \right) \right\|_F^2. \end{aligned}$$

By Thm. 2 in [49], we firstly obtain the t-SVD of $\mathbf{P}_{3-n} \left(\mathcal{A} \times_n \mathbf{D}_{I_n} - \frac{\mathcal{M}_n}{\rho} \right)$ as $\mathcal{U} \star \mathcal{S} \star \mathcal{V}^*$, then the solution to Eq. (III-C.8) is $\mathbf{P}_{3-n}^{-1}(\mathcal{U} \star \mathcal{T} \star \mathcal{V}^*)$ where \mathcal{T} is an f-diagonal tensor with

$$\begin{aligned} \overline{\mathcal{T}}[j, j, i] &= \arg \min_{x \geq 0} \psi(x) + \rho(x - \overline{\mathcal{S}}[j, j, i])^2 \\ i &= 1, 2, \dots, I_{3-n}, j = 1, 2, \dots, \min\{I_n, R\} \end{aligned}$$

which is solved via the generalized accelerated iterative [52], and the remaining elements being zero.

- Auxiliary variables: Following the convention of the ADMM framework, we update the multipliers as

$$\begin{aligned} \mathcal{M}_x &\leftarrow \mathcal{M}_x + \rho(\mathcal{X} - \mathcal{A} \times_1 \mathbf{P}_1 \times_2 \mathbf{P}_2 \times_3 \mathbf{S}), \\ \mathcal{M}_y &\leftarrow \mathcal{M}_y + \rho(\mathcal{Y} - \mathcal{A} \times_3 \mathbf{P}_3 \mathbf{S}), \\ \mathcal{M}_n &\leftarrow \mathcal{M}_n + \rho(\mathcal{G}_n - \mathcal{A} \times_n \mathbf{D}_{I_n}), n = 1, 2. \end{aligned} \quad (\text{III-C.9})$$

To help forcing convergence, we update the penalty parameter as $\rho \leftarrow \nu\rho$ where $\nu > 1$.

Algorithm 1 CMLpTR Optimization Algorithm

Input: The observed HSI \mathcal{X} , the MSI \mathcal{Y} , the spatial-degradation matrices \mathbf{P}_1 and \mathbf{P}_2 , the spectral-degradation matrix \mathbf{P}_3 , the subspace dimensionality R , the surrogate parameter γ .

Output: Estimated HSSI $\widehat{\mathcal{Z}}$.

- 1: Initialize penalty parameters $\rho > 0$, $\nu > 1$, the convergence tolerance $\epsilon > 0$, the difference matrices \mathbf{D}_{I_1} and \mathbf{D}_{I_2} .
 - 2: Set $\mathcal{A}, \mathcal{G}_1, \mathcal{G}_2, \mathcal{M}_1, \mathcal{M}_2, \mathcal{M}_x$ and \mathcal{M}_y to $\mathbf{0}$.
 - 3: $[\mathbf{S}, \sim, \sim] = \text{svds}(\mathcal{X}_{[3]}, R)$.
 - 4: **while** $\max \left\{ \left\| \mathcal{X} - \mathcal{A} \times_1 \mathbf{P}_1 \times_2 \mathbf{P}_2 \times_3 \mathbf{S} \right\|_F, \left\| \mathcal{Y} - \mathcal{A} \times_3 \mathbf{P}_3 \mathbf{S} \right\|_F, \left\{ \left\| \mathcal{G}_n - \mathcal{A} \times_n \mathbf{D}_{I_n} \right\|_F \right\}_{n=1}^2 \right\} > \epsilon$ **do**
 - 5: Update \mathcal{A} via Eq. (III-C.4).
 - 6: **for** $n = 1 : 2$ **do**
 - 7: Update \mathcal{G}_n via Eq. (III-C.8).
 - 8: **end for**
 - 9: Update $\mathcal{M}_1, \mathcal{M}_2, \mathcal{M}_x$ and \mathcal{M}_y via Eq. (III-C.9).
 - 10: $\rho \leftarrow \nu\rho$.
 - 11: **end while**
 - 12: $\widehat{\mathcal{Z}} \leftarrow \mathcal{A} \times_3 \mathbf{S}$.
-

D. Complexity and Convergence Analysis

The overall optimization algorithm is summarized in Alg. 1. In the updating of the spatial tensor \mathcal{A} , the main complexity lies in the calculation of the gradient, *i.e.*, Eq. (III-C.5), whose complexity is

$$\begin{aligned} C_1 \triangleq & \mathcal{O} \left(2 * (I_1^2 I_2 R + I_1 I_2^2 R) + R^2 I_1 I_2 + i_1 i_2 I_1 I_3 \right. \\ & \left. + i_2 I_1 I_2 I_3 + I_1 I_2 I_3 R + i_3 I_1 I_2 R + (I_1 - 1) I_1 I_2 R \right. \\ & \left. + I_1 (I_2 - 1) I_2 R \right) \\ = & \mathcal{O} \left(i_1 i_2 I_1^2 I_2^2 I_3 R^2 \right). \end{aligned}$$

To update the auxiliary variables \mathcal{G}_1 and \mathcal{G}_2 , their t-SVDs drive the complexity, which in total is

$$\begin{aligned} C_2 \triangleq & \mathcal{O} \left((I_1 (I_2 - 1) + I_2 (I_1 - 1)) R^2 \right) \\ = & \mathcal{O} \left(I_1 I_2 R^2 \right). \end{aligned}$$

The last part of the complexity comes from the tensor-matrix product in the updating of multipliers, *i.e.*, Eq. (III-C.9):

$$\begin{aligned} C_3 \triangleq & \mathcal{O} \left(I_1 I_2 R (i_1 + i_2 + i_3 + I_1 - 1 + I_2 - 1 + I_3) \right) \\ = & \mathcal{O} \left(i_1 i_2 i_3 I_1^2 I_2^2 I_3 R^2 \right). \end{aligned}$$

Therefore, the overall complexity of Alg. 1 is

$$C_1 + C_2 + C_3 = \mathcal{O} \left(i_1 i_2 i_3 I_1^2 I_2^2 I_3 R^2 \right).$$

Alg. 1 does not fall into any category of an existing convergence-guaranteed optimization paradigm. Its rough structure resembles the ADMM framework while the solution to some subproblems is customized following the LADMM.

Besides, the employment of non-convex surrogate brings more challenges to its convergence issue. Hence, we provide a rigorous convergence analysis below.

Theorem III-D.1: Denoting the sequence generated by Alg. 1 as:

$$\mathfrak{S}_t = \left\{ \mathcal{A}_t, \{\mathcal{G}_{n,t}\}_{n=1,2}, \mathcal{M}_{x,t}, \mathcal{M}_{y,t}, \{\mathcal{M}_{n,t}\}_{n=1,2} \right\}_{t \in \mathbb{N}},$$

given the boundedness of $\{\mathcal{M}_{x,t}, \mathcal{M}_{y,t}\}$, it follows that:

- (1) $\left\{ \mathcal{A}_t, \{\mathcal{G}_{n,t}\}_{n=1,2} \right\}_{t \in \mathbb{N}}$ is Cauchy sequence,
- (2) \mathfrak{S}_t is bounded,
- (3) Any accumulation point of \mathfrak{S}_t , denoted as

$$\mathfrak{S}_* = \left\{ \mathcal{A}_*, \{\mathcal{G}_{n,*}\}_{n=1,2}, \mathcal{M}_{x,*}, \mathcal{M}_{y,*}, \{\mathcal{M}_{n,*}\}_{n=1,2} \right\},$$

is a KKT point, *i.e.*, it satisfies

$$\begin{cases} \mathcal{M}_{n,*} \in -\frac{1}{2} \partial \|\mathcal{G}_{n,*}\|_{3-n, \psi}, n = 1, 2, \\ \nabla L_1(\mathcal{A}_*) = 0, \\ \mathcal{X} = \mathcal{A}_* \times_1 \mathbf{P}_1 \times_2 \mathbf{P}_2 \times_3 \mathbf{S}, \\ \mathcal{Y} = \mathcal{A}_* \times_3 \mathbf{P}_3 \mathbf{S}, \\ \mathcal{G}_{n,*} = \mathcal{A}_* \times_n \mathbf{D}_{I_n}, n = 1, 2. \end{cases}$$

Proof: Deferred to Sec. II in Appendix. ■

IV. EXPERIMENTS

In this section, we empirically validate the proposed method's effectiveness for the HSR task. Both non-blind and blind HSR are tested, among which the degradation matrices for blind HSR are estimated via [9]. Unsupervised state-of-the-art methods, including model-based Hysure [9], LTTR [18], LRTA [22], ASLA [25], GTNN [20] and data-driven SURE [33], ZSL [35] are involved for comparison. All model-based methods are implemented in MATLAB R2020b on Intel® Core™ i5-1135G7 CPU @ 2.40 GHz with 16-GB RAM, while the data-driven ones are implemented by Python 3.11.5 with Pytorch 1.10.2 on an NVIDIA RTX 3090 GPU with 24-GB RAM. The performance is measured in terms of peak signal-to-noise ratio (PSNR), relative dimensionless global error synthesis (ERGAS), spectral angle mapper (SAM), and structural similarity metric (SSIM) [53]. The higher the PSNR and SSIM, the better the performance. The lower the ERGAS and SAM, the higher the performance. Ideal values are $+\infty$, 0, 0, and 1 for PSNR, ERGAS, SAM, and SSIM, respectively.

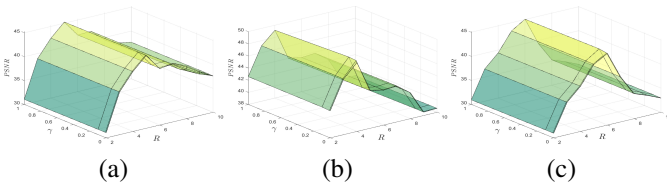


Fig. 2: Hyperparameter sensitivity reflected by the PSNR results for non-blind fusion on (a) URBAN; (b) Houston; (c) WDC.

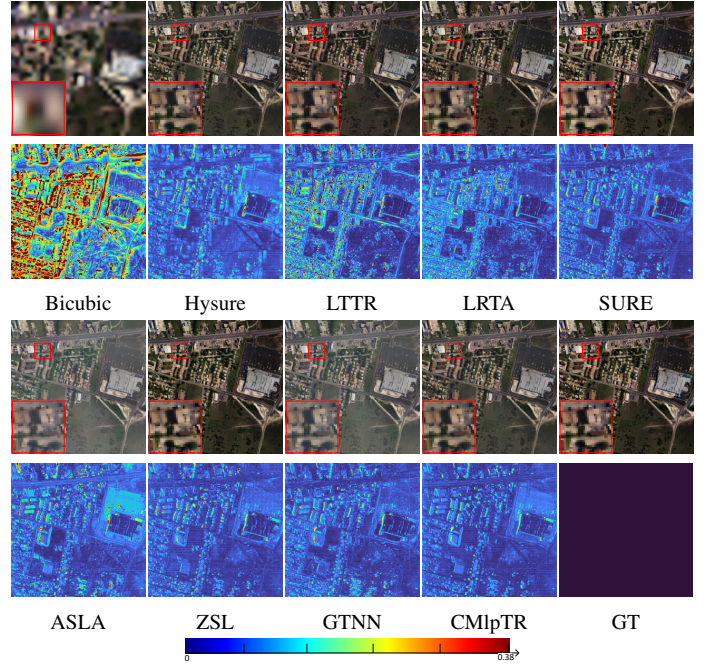


Fig. 3: Non-blind fusion results and error maps on the URBAN dataset. Pseudo-color is composed of bands 40, 30 and 10. Error maps are calculated by the pixel-wise SAM.

A. Datasets Description

Three hyperspectral datasets, *i.e.*, URBAN¹, Houston², and Washington DC (WDC)³ are employed. The URBAN dataset comprises a 210-band HSI with 307×307 pixels at 2-meter spatial resolution, covering the spectral range of 400-2500nm at 10nm intervals. After removing bands 1-4, 76, 87, 101-111, 136-153, and 198-210 due to water vapor and atmospheric interference, we extracted a $256 \times 256 \times 162$ HSSI from the upper-left corner of the processed data.

The Houston dataset consists of an HSI with 349×1905 spatial pixels and 144 spectral bands at 2.5-meter resolution, covering the 380-1050nm spectral range. With zero-valued pixels being discarded, we generated a $322 \times 1903 \times 144$ image cube, from which we crop off a $256 \times 256 \times 144$ subscene to serve as the HSSI. Besides, since the original image appears dark, we performed Gamma-calibration on the generated HSSI \mathcal{Z} to obtain $\mathcal{Z}^{0.7}$ as the ground-truth (GT) HSSI, where the power was calculated element-wisely.

The WDC dataset is acquired via the same sensor as URBAN. Hence, they have the same spatial and spectral resolutions and quality. Thus, we preprocessed the WDC dataset in the same way as URBAN to obtain a $256 \times 256 \times 162$ HSSI.

For each HSSI, we applied a 9×9 Gaussian kernel with a standard deviation of 3.3973 to blur it, followed by spatial downsampling by a factor of eight, resulting in an HSI of

¹<https://www.erdc.usace.army.mil/Media/Fact-Sheets/Fact-Sheet-Article-View/Article/610433/hypercube/#>

²https://hyperspectral.ee.uh.edu/?page_id=459

³<https://github.com/liangjiandeng/HyperPanCollection>

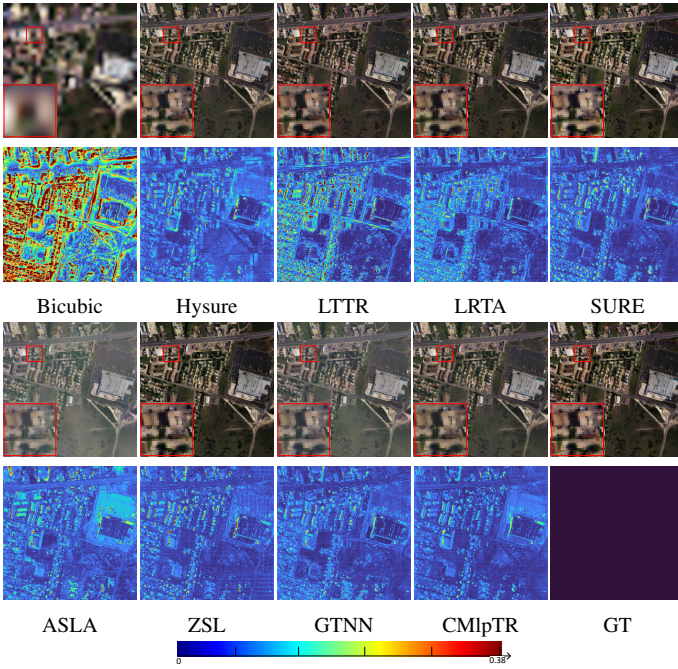


Fig. 4: Blind fusion results and error maps on the URBAN dataset. Pseudo-color is composed of bands 40, 30 and 10. Error maps are calculated by the pixel-wise SAM.

TABLE I: Numerical performance on the URBAN dataset. Best results are in boldface.

| Methods | Setup | | | | | | | |
|---------|-----------------|--------------------|------------------|-----------------|-----------------|--------------------|------------------|-----------------|
| | Non-blind | | | | Blind | | | |
| | PSNR \uparrow | ERGAS \downarrow | SAM \downarrow | SSIM \uparrow | PSNR \uparrow | ERGAS \downarrow | SAM \downarrow | SSIM \uparrow |
| Bicubic | 22.4646 | 5.8732 | 10.6064 | 0.4115 | 22.4646 | 5.8732 | 10.6064 | 0.4115 |
| Hysure | 42.9189 | 0.6890 | 2.9550 | 0.9920 | 42.7903 | 0.6778 | 2.9662 | 0.9920 |
| LTTR | 43.9124 | 0.8584 | 3.7677 | 0.9790 | 43.7321 | 0.8516 | 3.7948 | 0.9789 |
| LRTA | 44.5726 | 0.7171 | 2.8548 | 0.9873 | 44.3073 | 0.7187 | 2.8630 | 0.9873 |
| SURE | 42.9270 | 0.6169 | 2.4358 | 0.9915 | 42.7237 | 0.6326 | 2.5093 | 0.9914 |
| ASLA | 44.6256 | 0.6703 | 2.8596 | 0.9917 | 44.3815 | 0.6803 | 2.7664 | 0.9920 |
| ZSL | 43.1704 | 0.6226 | 2.4037 | 0.9927 | 42.9792 | 0.6431 | 2.5551 | 0.9921 |
| GTNN | 44.6832 | 0.5864 | 2.3858 | 0.9914 | 44.5186 | 0.5963 | 2.3980 | 0.9914 |
| CMlpTR | 45.2351 | 0.5588 | 2.2375 | 0.9947 | 45.1130 | 0.5610 | 2.2425 | 0.9947 |

spatial size 32×32 . For URBAN and WDC, the MSI of size $256 \times 256 \times 6$ was generated by averaging HSSI bands within six spectral ranges (450–520nm, 520–600nm, 630–690nm, 760–900nm, 1550–1750nm, and 2080–2350nm) to match the spectral response of the USGS/NASA Landsat 7 satellite [48]. As for Houston, the corresponding $256 \times 256 \times 4$ MSI was generated via an IKONOS-like reflectance spectral response filter [24].

B. Experimental Results

1) *Hyperparameter Sensitivity*: The main hyperparameters include the dimensionality of the spectral subspace, *i.e.*, R that captures the spectral low-rankness of the latent HSSI, and the surrogate parameter γ from $\psi(x) = \frac{\log(\gamma x + 1)}{\log(\gamma + 1)}$. To determine their values, we examine the PSNR sensitivity in non-blind fusion to both R and γ . The results are visualized in Fig. 2. It is clear to see that the proposed model is much more sensitive to R than to γ . From the distinct peak lines regarding R , it is easy to set R to five, four and six for URBAN, Houston and WDC,

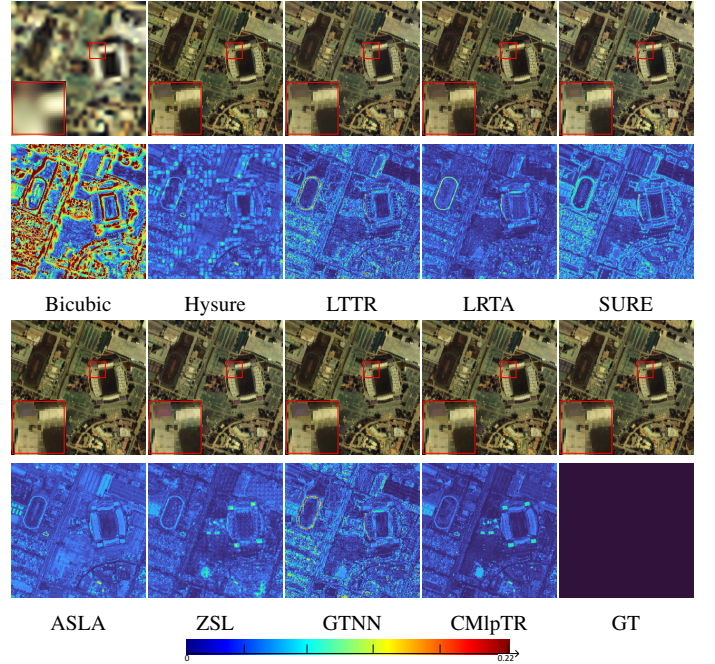


Fig. 5: Non-blind fusion results and error maps on the Houston dataset. Pseudo-color is composed of bands 45, 25 and 10. Error maps are calculated by the pixel-wise SAM.

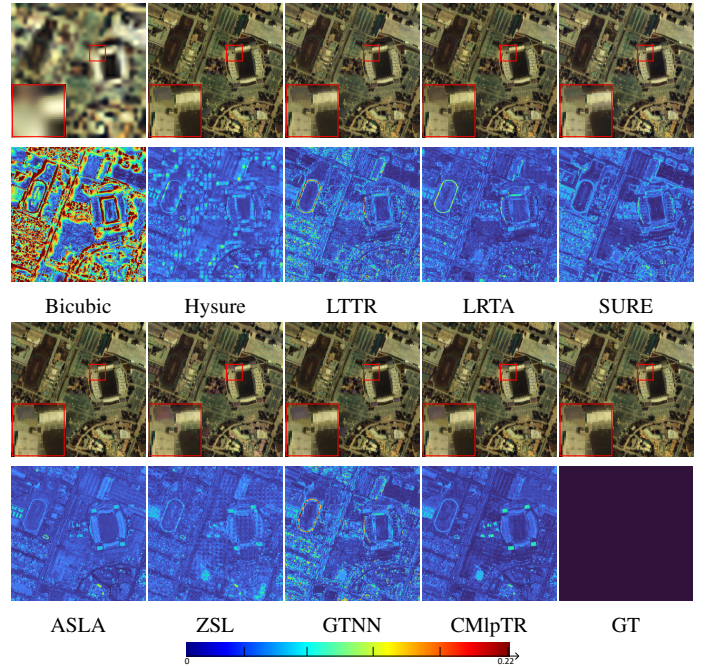


Fig. 6: Blind fusion results and error maps on the Houston dataset. Pseudo-color is composed of bands 45, 25 and 10. Error maps are calculated by the pixel-wise SAM.

respectively. As for γ , though the performance with respect to it remains relatively steady, there exists a black edge in each of the three surfaces at one common position where $\gamma = 0.1$. The corresponding PSNR value is higher than its neighbors if R is kept optimal. Thus, throughout these experiments, we set γ to 0.1.

TABLE II: Numerical performance on the Houston dataset. Best results are in boldface.

| Methods | Setup | | | | | | | |
|---------|-----------------|--------------------|------------------|-----------------|-----------------|--------------------|------------------|-----------------|
| | Non-blind | | | | Blind | | | |
| | PSNR \uparrow | ERGAS \downarrow | SAM \downarrow | SSIM \uparrow | PSNR \uparrow | ERGAS \downarrow | SAM \downarrow | SSIM \uparrow |
| Bicubic | 27.9764 | 2.8896 | 6.5494 | 0.6230 | 27.9764 | 2.8896 | 6.5494 | 0.6230 |
| Hysure | 48.2238 | 0.5736 | 1.4917 | 0.9927 | 46.3990 | 0.5866 | 1.5930 | 0.9922 |
| LTTR | 48.1071 | 0.5894 | 1.6414 | 0.9793 | 46.8301 | 0.5943 | 1.7098 | 0.9793 |
| LRTA | 46.7599 | 0.4785 | 1.1938 | 0.9922 | 46.5129 | 0.4790 | 1.3003 | 0.9919 |
| SURE | 44.3703 | 0.8480 | 1.6479 | 0.9769 | 44.8562 | 0.7868 | 1.4291 | 0.9829 |
| ASLA | 48.7790 | 0.8554 | 1.5664 | 0.9933 | 47.6438 | 0.7465 | 1.3068 | 0.9943 |
| ZSL | 46.1368 | 0.5463 | 1.1997 | 0.9911 | 45.5776 | 0.5667 | 1.3697 | 0.9912 |
| GTNN | 48.2029 | 0.5980 | 1.5338 | 0.9851 | 46.7844 | 0.6262 | 1.6013 | 0.9848 |
| CMlPTr | 49.7612 | 0.4334 | 0.9367 | 0.9953 | 48.4184 | 0.4591 | 1.0784 | 0.9946 |

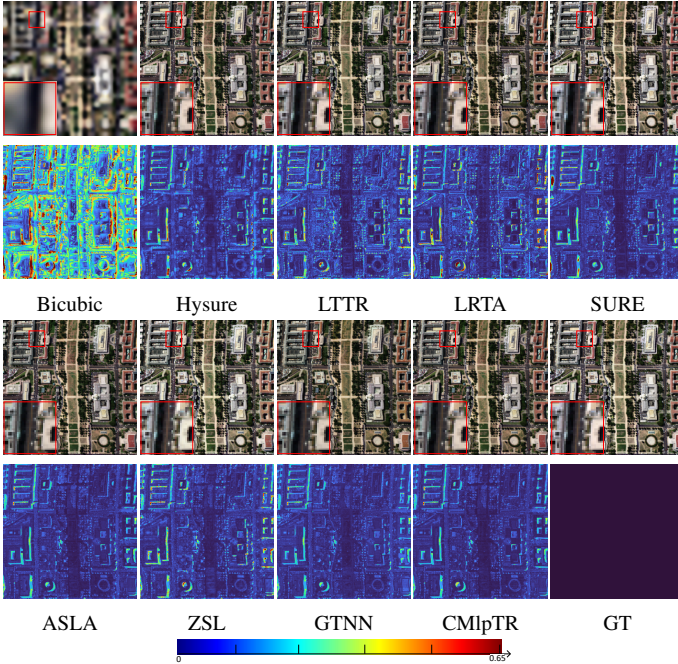


Fig. 7: Non-blind fusion results and error maps on the WDC dataset. Pseudo-color is composed of bands 40, 30 and 20. Error maps are calculated by the pixel-wise SAM.

2) *HSR Results on URBAN Dataset*: The visual results are displayed in Figs. 3 and 4. In the non-blind results, all methods end up with fine spatial details, only ASLA and GTNN exhibit slight color deviations and appear hazy. Besides, SURE, ZSL, GTNN and the proposed CMlPTr generate the most darkest error maps, among which our CMlPTr is the best at suppressing higher error values. Similar conclusions can be drawn from the blind results in Fig. 4, except that all error maps have become brighter due to the estimation inaccuracies in the degradation matrices. The conclusions above are further strengthened by the numerical results in Tab. I, in which the proposed CMlPTr yielded the best values on all indexes, while

SURE, ZSL and GTNN are the most competitive having a look at the SAM metric.

3) *HSR Results on Houston Dataset*: The results on the Houston dataset are depicted in Figs. 5-6 and numerically reported in Tab. II. By the overall brightness of the error maps, it appears that ASLA, ZSL and the proposed CMlPTr deliver the closest reconstruction. However, ZSL suffers from block-like artifacts and ASLA is not as good as our CMlPTr in background suppression. Even though TV constraints are considered in ASLA, the multi-constraint paradigm leaves the problem of mutual interference. Besides, hinted by the numerical results in Tab. II, it is noticed that LRTA is better at reconstructing the bright regions in our CMlPTr's error map, leading to its competitiveness observing the SAM metric, even though LRTA shows random high-error pixels due to the neglect of TV priors.

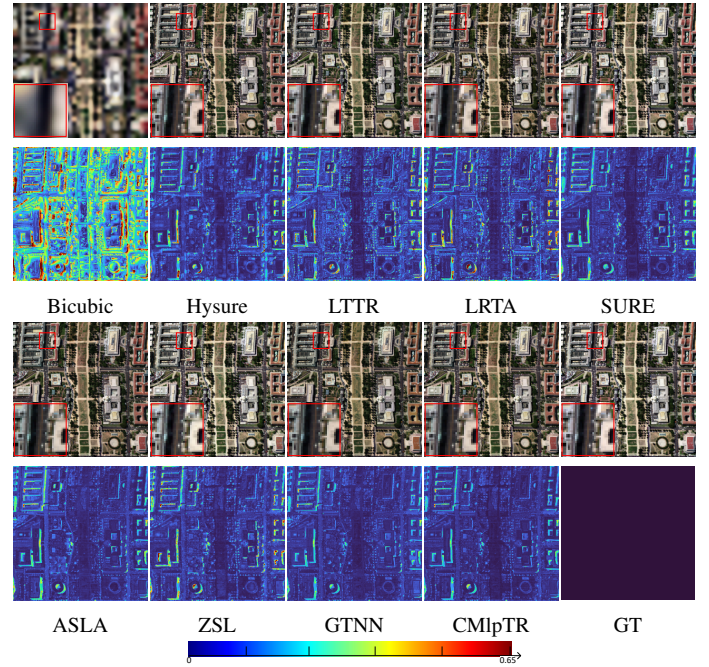


Fig. 8: Blind fusion results and error maps on the WDC dataset. Pseudo-color is composed of bands 40, 30 and 20. Error maps are calculated by the pixel-wise SAM.

TABLE III: Numerical performance on the WDC dataset. Best results are in boldface.

| Methods | Setup | | | | | | | |
|---------|-----------------|--------------------|------------------|-----------------|-----------------|--------------------|------------------|-----------------|
| | Non-blind | | | | Blind | | | |
| | PSNR \uparrow | ERGAS \downarrow | SAM \downarrow | SSIM \uparrow | PSNR \uparrow | ERGAS \downarrow | SAM \downarrow | SSIM \uparrow |
| Bicubic | 19.6920 | 7.1549 | 12.3534 | 0.2588 | 19.6920 | 7.1549 | 12.3534 | 0.2588 |
| Hysure | 43.6645 | 0.6142 | 3.2399 | 0.9936 | 43.4473 | 0.6048 | 3.2742 | 0.9935 |
| LTTR | 42.9732 | 0.7308 | 3.5122 | 0.9886 | 42.7777 | 0.7406 | 3.6109 | 0.9883 |
| LRTA | 43.8438 | 0.6604 | 3.6210 | 0.9890 | 43.6905 | 0.6624 | 3.6378 | 0.9890 |
| SURE | 42.2816 | 0.5884 | 2.9213 | 0.9931 | 42.0958 | 0.5961 | 2.8804 | 0.9928 |
| ASLA | 45.1584 | 0.5735 | 2.4119 | 0.9958 | 44.3206 | 0.5838 | 2.7515 | 0.9950 |
| ZSL | 42.3886 | 0.5939 | 2.9659 | 0.9935 | 42.9526 | 0.6144 | 3.1297 | 0.9932 |
| GTNN | 43.2923 | 0.5920 | 2.5136 | 0.9949 | 43.2412 | 0.5917 | 2.5163 | 0.9949 |
| CMlPTr | 45.0320 | 0.4819 | 2.2969 | 0.9959 | 44.9592 | 0.4817 | 2.2971 | 0.9959 |

4) *HSR Results on WDC Dataset*: The results on the WDC dataset are depicted in Figs. 7-8 and numerically reported in

Tab. II. These visual results demonstrate that the WDC dataset presents greater textural complexity compared to the other two datasets, as evidenced by the pronounced high-frequency patterns in the error maps and the extended dynamic range of the colorbar. In Tab. III, the proposed CMlpTR performs the best while ASLA turns out to be the most competitive achieving the best PSNR value in the non-blind experiment. The visual results agree with the numerical ones, where ASLA, GTNN and CMlpTR obtain the darkest error maps.

V. CONCLUSION

This paper raised the attention on the difficulty in the co-representation of multi-level-priors in the HSR task. Through the proposal of our NMS-t-CTV and combining it with the BTd, we achieved compact and tight representations of multi-level and multi-dimensional structural correlations inherent in HSSI while maintaining theoretical soundness. To efficiently solve the resulting high-dimensional optimization problem, a LADMM-inspired algorithm was customized, with convergence guarantees established under practical boundedness conditions. The compactness of the proposed model not only facilitated convergence analysis but also saved it from the problem of mutual-interference between multiple constraints. Extensive experiments on both non-blind and blind HSR tasks demonstrated the practical effectiveness of the proposed approach, showing improved performance in preserving spectral-spatial details while keeping computational demands manageable.

APPENDIX

A. Proof of Prop. III-B.1

Proof: In analogy with the proof architecture of Prop. 2 in the Supplementary Material of [37], on one hand, we have

$$\begin{aligned}
& \text{rank}_{3-t}(\mathcal{A} \times_n \mathbf{D}_{I_n}) \\
&= \text{rank}_{3-t}(\mathcal{Z} \times_n \mathbf{D}_{I_n} \times_3 \mathbf{S}^*) \\
&= \max_{i \in \{1, 2, \dots, I_{3-n}\}} \text{rank}(\overline{\mathbb{P}_{3-n}(\mathcal{Z} \times_n \mathbf{D}_{I_n} \times_3 \mathbf{S}^*)}_{:, :, i}) \\
&= \max_{i \in \{1, 2, \dots, I_{3-n}\}} \text{rank}(\overline{\mathbf{D}_{I_n} \mathbb{P}_{3-n}(\mathcal{Z})}_{:, :, i} \mathbf{S}^*) \\
&= \max_{i \in \{1, 2, \dots, I_{3-n}\}} \text{rank}(\overline{\mathbf{D}_{I_n} \mathbb{P}_{3-n}(\mathcal{Z})}_{:, :, i}) \\
&\geq \max_{i \in \{1, 2, \dots, I_{3-n}\}} \left\{ \text{rank}(\mathbf{D}_{I_n}) + \text{rank}(\overline{\mathbb{P}_{3-n}(\mathcal{Z})}_{:, :, i}) - I_n \right\} \\
&= \max_{i \in \{1, 2, \dots, I_{3-n}\}} \left\{ \text{rank}(\overline{\mathbb{P}_{3-n}(\mathcal{Z})}_{:, :, i}) - 1 \right\} \\
&= \text{rank}_{3-t}(\mathcal{Z}) - 1.
\end{aligned}$$

On the other hand,

$$\begin{aligned}
\text{rank}_{3-t}(\mathcal{A} \times_n \mathbf{D}_{I_n}) &= \max_{i \in \{1, 2, \dots, I_{3-n}\}} \text{rank}(\overline{\mathbf{D}_{I_n} \mathbb{P}_{3-n}(\mathcal{Z})}_{:, :, i}) \text{ which leads to} \\
&\leq \max_{i \in \{1, 2, \dots, I_{3-n}\}} \text{rank}(\overline{\mathbb{P}_{3-n}(\mathcal{Z})}_{:, :, i}) \\
&= \text{rank}_{3-t}(\mathcal{Z}).
\end{aligned}$$

Thus, Eq. (III-B.2) is proven. We proceed to prove Eq. (III-B.3). Denoting $\mathcal{G}_n = \mathcal{A} \times_n \mathbf{D}_{I_n}$, let $\mathcal{U} \star \mathcal{S} \star \mathcal{V}^*$ be the t-SVD of $\mathbb{P}_{3-n}(\mathcal{G}_n) = \text{permute}(\mathcal{G}_n, [n, 3, 3-n])$, then we can write

$$\|\mathcal{G}_n\|_{3-t, \psi} = \frac{1}{I_{3-n}} \sum_{i=1}^{I_{3-n}} \sum_{j=1}^{\min\{I_n, R\}} \psi(\overline{\mathcal{S}}[j, j, i]).$$

Since \mathcal{A} is bounded, $\exists x_B > 0$, such that $\overline{\mathcal{S}}[j, j, i] \leq x_B, \forall i, j$. Let $b = \frac{\psi(x_B)}{x_B}$, then based on the properties of $\psi(\cdot)$, $\psi(\overline{\mathcal{S}}[j, j, i]) \geq b \overline{\mathcal{S}}[j, j, i], \forall i, j$. Thereupon,

$$\begin{aligned}
\|\mathcal{G}_n\|_{3-t, \psi} &= \frac{1}{I_{3-n}} \sum_{i=1}^{I_{3-n}} \sum_{j=1}^{\min\{I_n, R\}} \psi(\overline{\mathcal{S}}[j, j, i]) \\
&\geq \frac{b}{I_{3-n}} \sum_{i=1}^{I_{3-n}} \sum_{j=1}^{\min\{I_n, R\}} \overline{\mathcal{S}}[j, j, i] \\
&= \frac{b}{I_{3-n}} \left\| \overline{\mathbb{P}_{3-n}(\mathcal{G}_n)} \right\|_* \\
&= \frac{b}{I_{3-n}} \left\| \overline{\mathbb{P}_{3-n}(\mathcal{G}_n)} \right\|_F \\
&\geq \frac{b}{\sqrt{I_{3-n}}} \|\mathbb{P}_{3-n}(\mathcal{G}_n)\|_F \\
&\geq \frac{b}{\sqrt{I^m}} \|\mathcal{G}_n\|_F \\
&\geq \frac{b}{\sqrt{I^m I_1 I_2 R}} \|\mathcal{G}_n\|_1
\end{aligned}$$

where $I^m \triangleq \max\{I_1, I_2\}$. It then follows that:

$$\begin{aligned}
\|\mathcal{A}\|_{*, \psi} &\geq \frac{b}{2\sqrt{I^m}} \|\mathcal{A}\|_{TV}, \\
\|\mathcal{A}\|_{*, \psi} &\geq \frac{b}{2\sqrt{I^m I_1 I_2 R}} \|\mathcal{A}\|_{ATV}.
\end{aligned}$$

Furthermore, let $g \triangleq \overline{\lim}_{x \rightarrow 0^+} \psi(x)$, then based on the properties of $\psi(\cdot)$, we have $\psi(\overline{\mathcal{S}}[j, j, i]) \leq g \overline{\mathcal{S}}[j, j, i]$. Then, it is derived that:

$$\begin{aligned}
\|\mathcal{G}_n\|_{3-t, \psi} &= \frac{1}{I_{3-n}} \sum_{i=1}^{I_{3-n}} \sum_{j=1}^{\min\{I_n, R\}} \psi(\overline{\mathcal{S}}[j, j, i]) \\
&\leq \frac{g}{I_{3-n}} \sum_{i=1}^{I_{3-n}} \sum_{j=1}^{\min\{I_n, R\}} \overline{\mathcal{S}}[j, j, i] \\
&= \frac{g}{I_{3-n}} \left\| \overline{\mathbb{P}_{3-n}(\mathcal{G}_n)} \right\|_* \\
&\leq g \sqrt{\frac{\min\{I_n, R\}}{I_{3-n}}} \left\| \overline{\mathbb{P}_{3-n}(\mathcal{G}_n)} \right\|_F \\
&= g \sqrt{\min\{I_n, R\}} \|\mathbb{P}_{3-n}(\mathcal{G}_n)\|_F \\
&= g \sqrt{\min\{I_n, R\}} \|\mathcal{G}_n\|_F \\
&\leq g \sqrt{\min\{I_n, R\}} \|\mathcal{G}_n\|_1,
\end{aligned}$$

$$\|\mathcal{A}\|_{*, \psi} \leq g \sqrt{2 \min\{I_n, R\}} \|\mathcal{A}\|_{TV},$$

$$\|\mathcal{A}\|_{*, \psi} \leq g \sqrt{\min\{I_n, R\}} \|\mathcal{A}\|_{ATV}.$$

Hence, Eq. (III-B.3) is proven. \blacksquare

B. Proof of Thm. III-D.1

Proof: Proof of (1) and (2): According to the optimality of subproblem (III-C.8), it holds in the $(t+1)$ th iteration that:

$$0 \in \partial \|\mathcal{G}_{n,t+1}\|_{3_{*}^{-n},\psi} + 2\rho_t \left(\mathcal{G}_{n,t+1} + \frac{\mathcal{M}_{n,t}}{\rho_t} - \mathcal{A}_{t+1} \times_n \mathbf{D}_{I_n} \right)$$

where $\partial \|\mathcal{G}_{n,t+1}\|_{3_{*}^{-n},\psi}$ denotes the subdifferential of $\|\cdot\|_{3_{*}^{-n},\psi}$ at $\mathcal{G}_{n,t+1}$, whose existence is guaranteed by Lemma A1 in the Supplementary Material of [47], which together with **P1** and **P2** results in the boundedness of $\partial \|\mathcal{G}_{n,t+1}\|_{3_{*}^{-n},\psi}$. Further exploiting the updating rule of \mathcal{M}_n , it is derived that:

$$\mathcal{M}_{n,t+1} \in -\frac{1}{2} \partial \|\mathcal{G}_{n,t+1}\|_{3_{*}^{-n},\psi} \quad (\text{B.1})$$

Thus, $\mathcal{M}_{n,t+1}$ is bounded. Moreover, by the updating rule (III-C.4),

$$\begin{aligned} & \tau (\mathcal{A}_{t+1} - \mathcal{A}_t) \quad (\text{B.2}) \\ &= -\nabla L_1(\mathcal{A}_t) \\ &= -2 \left(\mathcal{A}_t \times_1 \mathbf{P}_1^* \mathbf{P}_1 \times_2 \mathbf{P}_2^* \mathbf{P}_2 + \mathcal{A}_t \times_3 \mathbf{S}^* \mathbf{P}_3^* \mathbf{P}_3 \mathbf{S} + \right. \\ & \quad \sum_{n=1}^2 \mathcal{A}_t \times_n \mathbf{D}_{I_n}^* \mathbf{D}_{I_n} - \left(\mathcal{X} + \frac{\mathcal{M}_{x,t}}{\rho_t} \right) \times_1 \mathbf{P}_1^* \\ & \quad \times_2 \mathbf{P}_2^* \times_3 \mathbf{S}^* - \left(\mathcal{Y} + \frac{\mathcal{M}_{y,t}}{\rho_t} \right) \times_3 \mathbf{S}^* \mathbf{P}_3^* \\ & \quad \left. - \sum_{n=1}^2 \left(\mathcal{G}_{n,t} + \frac{\mathcal{M}_{n,t}}{\rho_t} \right) \times_n \mathbf{D}_{I_n}^* \right). \quad (\text{B.3}) \end{aligned}$$

By the updating rule of \mathcal{M}_x ,

$$\mathcal{X} + \frac{\mathcal{M}_{x,t}}{\rho_t} = \frac{\mathcal{M}_{x,t+1}}{\rho_t} + \mathcal{A}_{t+1} \times_1 \mathbf{P}_1 \times_2 \mathbf{P}_2 \times_3 \mathbf{S}.$$

Then

$$\begin{aligned} & \mathcal{A}_t \times_1 \mathbf{P}_1^* \mathbf{P}_1 \times_2 \mathbf{P}_2^* \mathbf{P}_2 - \left(\mathcal{X} + \frac{\mathcal{M}_{x,t}}{\rho_t} \right) \times_1 \mathbf{P}_1^* \times_2 \mathbf{P}_2^* \\ & \times_3 \mathbf{S}^* = (\mathcal{A}_t - \mathcal{A}_{t+1}) \times_1 \mathbf{P}_1^* \mathbf{P}_1 \times_2 \mathbf{P}_2^* \mathbf{P}_2 \\ & \quad - \frac{\mathcal{M}_{x,t+1} \times_1 \mathbf{P}_1^* \times_2 \mathbf{P}_2^* \times_3 \mathbf{S}^*}{\rho_t}. \quad (\text{B.4}) \end{aligned}$$

Similarly, by the updating rule of \mathcal{M}_y ,

$$\mathcal{Y} + \frac{\mathcal{M}_{y,t}}{\rho_t} = \frac{\mathcal{M}_{y,t+1}}{\rho_t} + \mathcal{A}_{t+1} \times_3 \mathbf{P}_3 \mathbf{S}.$$

Then

$$\begin{aligned} & \mathcal{A}_t \times_3 \mathbf{S}^* \mathbf{P}_3^* \mathbf{P}_3 \mathbf{S} - \left(\mathcal{Y} + \frac{\mathcal{M}_{y,t}}{\rho_t} \right) \times_3 \mathbf{S}^* \mathbf{P}_3^* \\ &= (\mathcal{A}_t - \mathcal{A}_{t+1}) \times_3 \mathbf{S}^* \mathbf{P}_3^* \mathbf{P}_3 \mathbf{S} - \frac{\mathcal{M}_{y,t+1} \times_3 \mathbf{S}^* \mathbf{P}_3^*}{\rho_t}. \quad (\text{B.5}) \end{aligned}$$

Subsequently, we invoke the updating rule of \mathcal{M}_n to obtain

$$\frac{\mathcal{M}_{n,t}}{\rho_t} = \frac{\mathcal{M}_{n,t+1}}{\rho_t} + \mathcal{A}_{t+1} \times_n \mathbf{D}_{I_n} - \mathcal{G}_{n,t+1}.$$

Then

$$\mathcal{A}_t \times_n \mathbf{D}_{I_n}^* \mathbf{D}_{I_n} - \left(\mathcal{G}_{n,t} + \frac{\mathcal{M}_{n,t}}{\rho_t} \right) \times_n \mathbf{D}_{I_n}^*$$

$$\begin{aligned} &= (\mathcal{A}_t - \mathcal{A}_{t+1}) \times_n \mathbf{D}_{I_n}^* \mathbf{D}_{I_n} \\ & \quad - \left(\mathcal{G}_{n,t} - \mathcal{G}_{n,t+1} + \frac{\mathcal{M}_{n,t+1}}{\rho_t} \right) \times_n \mathbf{D}_{I_n}^*. \quad (\text{B.6}) \end{aligned}$$

We then use the updating rule of \mathcal{M}_n again to yield

$$\begin{aligned} \mathcal{G}_{n,t} &= \frac{\mathcal{M}_{n,t} - \mathcal{M}_{n,t-1}}{\rho_{t-1}} + \mathcal{A}_t \times_n \mathbf{D}_{I_n}, \\ \mathcal{G}_{n,t+1} &= \frac{\mathcal{M}_{n,t+1} - \mathcal{M}_{n,t}}{\rho_t} + \mathcal{A}_{t+1} \times_n \mathbf{D}_{I_n}, \end{aligned}$$

from which it follows

$$\begin{aligned} \mathcal{G}_{n,t} - \mathcal{G}_{n,t+1} &= \frac{(\nu+1)\mathcal{M}_{n,t} + \mathcal{M}_{n,t+1} - \nu\mathcal{M}_{n,t-1}}{\rho_t} \\ & \quad + (\mathcal{A}_t - \mathcal{A}_{t+1}) \times_n \mathbf{D}_{I_n}. \quad (\text{B.7}) \end{aligned}$$

Taking Eq. (B.7) into Eq. (B.6), it is derived that:

$$\begin{aligned} & \mathcal{A}_t \times_n \mathbf{D}_{I_n}^* \mathbf{D}_{I_n} - \left(\mathcal{G}_{n,t} + \frac{\mathcal{M}_{n,t}}{\rho_t} \right) \times_n \mathbf{D}_{I_n}^* \\ &= -\frac{(\nu+1)\mathcal{M}_{n,t} + 2\mathcal{M}_{n,t+1} - \nu\mathcal{M}_{n,t-1}}{\rho_t} \times_n \mathbf{D}_{I_n}^*. \quad (\text{B.8}) \end{aligned}$$

Absorbing Eq. (B.4), Eq. (B.5) and Eq. (B.8) into Eq. (B.3), we have

$$\begin{aligned} & \mathbb{H}(\mathcal{A}_{t+1} - \mathcal{A}_t) \\ &= 2 \left(\frac{\mathcal{M}_{x,t+1} \times_1 \mathbf{P}_1^* \times_2 \mathbf{P}_2^* \times_3 \mathbf{S}^*}{\rho_t} + \frac{\mathcal{M}_{y,t+1} \times_3 \mathbf{S}^* \mathbf{P}_3^*}{\rho_t} \right. \\ & \quad \left. + \sum_{n=1}^2 \frac{(\nu+1)\mathcal{M}_{n,t} + 2\mathcal{M}_{n,t+1} - \nu\mathcal{M}_{n,t-1}}{\rho_t} \times_n \mathbf{D}_{I_n}^* \right) \quad (\text{B.9}) \end{aligned}$$

where

$$\mathbb{H}(\mathcal{A}) = \tau \mathcal{A} - 2(\mathcal{A} \times_1 \mathbf{P}_1^* \mathbf{P}_1 \times_2 \mathbf{P}_2^* \mathbf{P}_2 + \mathcal{A} \times_3 \mathbf{S}^* \mathbf{P}_3^* \mathbf{P}_3 \mathbf{S})$$

for any $\mathcal{A} \in \mathbb{R}^{I_1 \times I_2 \times R}$. According to Eq. (III-C.7), it can be proven that $\mathbb{H}(\cdot)$ is an invertible linear mapping. Hence,

$$\begin{aligned} & \mathcal{A}_{t+1} - \mathcal{A}_t \\ &= 2\mathbb{H}^{-1} \left(\frac{\mathcal{M}_{x,t+1} \times_1 \mathbf{P}_1^* \times_2 \mathbf{P}_2^* \times_3 \mathbf{S}^*}{\rho_t} + \frac{\mathcal{M}_{y,t+1} \times_3 \mathbf{S}^* \mathbf{P}_3^*}{\rho_t} \right. \\ & \quad \left. + \sum_{n=1}^2 \frac{(\nu+1)\mathcal{M}_{n,t} + 2\mathcal{M}_{n,t+1} - \nu\mathcal{M}_{n,t-1}}{\rho_t} \times_n \mathbf{D}_{I_n}^* \right). \end{aligned}$$

Since $\left\{ \mathcal{M}_{x,t}, \mathcal{M}_{y,t}, \{\mathcal{M}_{n,t}\}_{n=1,2} \right\}_{t \in \mathbb{N}}$ is bounded and ρ_t is exponential, it is concluded that $\{\mathcal{A}_t\}_{t \in \mathbb{N}}$ is Cauchy sequence. Besides, from the updating rule of \mathcal{M}_n , we have

$$\begin{aligned} & \lim_{t \rightarrow \infty} \mathcal{G}_{n,t+1} \\ &= \lim_{t \rightarrow \infty} \frac{\mathcal{M}_{n,t+1} - \mathcal{M}_{n,t}}{\rho_t} + \mathcal{A}_{t+1} \times_n \mathbf{D}_{I_n} \\ &= \lim_{t \rightarrow \infty} \mathcal{A}_{t+1} \times_n \mathbf{D}_{I_n}. \end{aligned}$$

Hence $\left\{ \{\mathcal{G}_{n,t}\}_{n \in \{1,2\}} \right\}_{t \in \mathbb{N}}$ is also Cauchy sequence. We now have (1) and (2) proven.

Proof of (3): Recall that $\psi(x) = \frac{\log(\gamma x + 1)}{\log(\gamma + 1)}$, once again invoking Lemma A1 in the Supplementary Material of

[47], it is easy to conclude from Eq. (B.1) that $\mathcal{M}_{n,*} \in -\frac{1}{2}\partial \|\mathcal{G}_{n,*}\|_{3-n,*}^{\psi}$.

By Eq. (III-C.4), $\mathcal{A}_{t+1} - \mathcal{A}_t = \frac{\nabla L_1(\mathcal{A}_t)}{\tau}$. Taking $t \rightarrow \infty$, we have $\nabla L_1(\mathcal{A}_*) = 0$.

By Eq. (III-C.9),

$$\begin{aligned} \frac{\mathcal{M}_{x,t+1} - \mathcal{M}_{x,t}}{\rho_t} &= \mathcal{X} - \mathcal{A}_t \times_1 \mathbf{P}_1 \times_2 \mathbf{P}_2 \times_3 \mathbf{S}, \\ \frac{\mathcal{M}_{y,t+1} - \mathcal{M}_{y,t}}{\rho_t} &= \mathcal{Y} - \mathcal{A}_t \times_3 \mathbf{P}_3 \mathbf{S}, \\ \frac{\mathcal{M}_{n,t+1} - \mathcal{M}_{n,t}}{\rho_t} &= \mathcal{G}_n - \mathcal{A}_t \times_n \mathbf{D}_{I_n}, n = 1, 2. \end{aligned}$$

Taking $t \rightarrow \infty$, we have:

$$\begin{aligned} \mathcal{X} &= \mathcal{A}_* \times_1 \mathbf{P}_1 \times_2 \mathbf{P}_2 \times_3 \mathbf{S}, \\ \mathcal{Y} &= \mathcal{A}_* \times_3 \mathbf{P}_3 \mathbf{S}, \\ \mathcal{G}_{n,*} &= \mathcal{A}_* \times_n \mathbf{D}_{I_n}, n = 1, 2. \end{aligned}$$

-
- REFERENCES
- [1] Y. Su, L. Gao, M. Jiang, A. Plaza, X. Sun, and B. Zhang, "Nsckl: Normalized spectral clustering with kernel-based learning for semisupervised hyperspectral image classification," *IEEE Transactions on Cybernetics*, vol. 53, no. 10, pp. 6649–6662, 2023.
 - [2] H. Sima, J. Wang, P. Guo, J. Sun, H. Liu, M. Xu, and Y. Zou, "Composite kernel of mutual learning on mid-level features for hyperspectral image classification," *IEEE Transactions on Cybernetics*, vol. 52, no. 11, pp. 12217–12230, 2022.
 - [3] Z. Li, F. Xiong, J. Zhou, J. Lu, and Y. Qian, "Learning a deep ensemble network with band importance for hyperspectral object tracking," *IEEE Transactions on Image Processing*, vol. 32, pp. 2901–2914, 2023.
 - [4] W. Dong, X. Wu, J. Qu, P. Gamba, S. Xiao, A. Vizziello, and Y. Li, "Deep spatial–spectral joint-sparse prior encoding network for hyperspectral target detection," *IEEE Transactions on Cybernetics*, vol. 54, no. 12, pp. 7780–7792, 2024.
 - [5] C. Jiao, C. Chen, S. Gou, X. Wang, B. Yang, X. Chen, and L. Jiao, " ℓ_1 sparsity-regularized attention multiple-instance network for hyperspectral target detection," *IEEE Transactions on Cybernetics*, vol. 53, no. 1, pp. 124–137, 2023.
 - [6] G. Vivone, "Multispectral and hyperspectral image fusion in remote sensing: A survey," *Information Fusion*, vol. 89, pp. 405–417, 2023.
 - [7] N. Yokoya, C. Grohnfeldt, and J. Chanussot, "Hyperspectral and multispectral data fusion: A comparative review of the recent literature," *IEEE Geoscience and Remote Sensing Magazine*, vol. 5, no. 2, pp. 29–56, 2017.
 - [8] H. Song, B. Huang, K. Zhang, and H. Zhang, "Spatio-spectral fusion of satellite images based on dictionary-pair learning," *Information Fusion*, vol. 18, pp. 148–160, 2014.
 - [9] M. Simões, J. Bioucas-Dias, L. B. Almeida, and J. Chanussot, "A convex formulation for hyperspectral image superresolution via subspace-based regularization," *IEEE Transactions on Geoscience and Remote Sensing*, vol. 53, no. 6, pp. 3373–3388, 2015.
 - [10] Q. Wei, N. Dobigeon, and J.-Y. Tourneret, "Fast fusion of multi-band images based on solving a Sylvester equation," *IEEE Transactions on Image Processing*, vol. 24, no. 11, pp. 4109–4121, 2015.
 - [11] R. Dian, S. Li, L. Fang, and Q. Wei, "Multispectral and hyperspectral image fusion with spatial-spectral sparse representation," *Information Fusion*, vol. 49, pp. 262–270, 2019.
 - [12] J. Xue, Y.-Q. Zhao, Y. Bu, W. Liao, J. C.-W. Chan, and W. Philips, "Spatial-spectral structured sparse low-rank representation for hyperspectral image super-resolution," *IEEE Transactions on Image Processing*, vol. 30, pp. 3084–3097, 2021.
 - [13] M. Wang, D. Hong, Z. Han, J. Li, J. Yao, L. Gao, B. Zhang, and J. Chanussot, "Tensor decompositions for hyperspectral data processing in remote sensing: A comprehensive review," *IEEE Geoscience and Remote Sensing Magazine*, vol. 11, no. 1, pp. 26–72, 2023.
 - [14] T. G. Kolda and B. W. Bader, "Tensor decompositions and applications," *SIAM review*, vol. 51, no. 3, pp. 455–500, 2009.
 - [15] S. Li, R. Dian, L. Fang, and J. M. Bioucas-Dias, "Fusing hyperspectral and multispectral images via coupled sparse tensor factorization," *IEEE Transactions on Image Processing*, vol. 27, no. 8, pp. 4118–4130, 2018.
 - [16] R. Dian, S. Li, L. Fang, T. Lu, and J. M. Bioucas-Dias, "Nonlocal sparse tensor factorization for semiblind hyperspectral and multispectral image fusion," *IEEE Transactions on Cybernetics*, vol. 50, no. 10, pp. 4469–4480, 2020.
 - [17] Y. Chang, L. Yan, X.-L. Zhao, H. Fang, Z. Zhang, and S. Zhong, "Weighted low-rank tensor recovery for hyperspectral image restoration," *IEEE Transactions on Cybernetics*, vol. 50, no. 11, pp. 4558–4572, 2020.
 - [18] R. Dian, S. Li, and L. Fang, "Learning a low tensor-train rank representation for hyperspectral image super-resolution," *IEEE Transactions on Neural Networks and Learning Systems*, vol. 30, no. 9, pp. 2672–2683, 2019.
 - [19] I. V. Oseledets, "Tensor-train decomposition," *SIAM Journal on Scientific Computing*, vol. 33, no. 5, pp. 2295–2317, 2011.
 - [20] R. Dian, Y. Liu, and S. Li, "Hyperspectral image fusion via a novel generalized tensor nuclear norm regularization," *IEEE Transactions on Neural Networks and Learning Systems*, vol. 36, no. 4, pp. 7437–7448, 2025.
 - [21] M. E. Kilmer, K. Braman, N. Hao, and R. C. Hoover, "Third-order tensors as operators on matrices: A theoretical and computational framework with applications in imaging," *SIAM Journal on Matrix Analysis and Applications*, vol. 34, no. 1, pp. 148–172, 2013.
 - [22] N. Liu, L. Li, W. Li, R. Tao, J. E. Fowler, and J. Chanussot, "Hyperspectral restoration and fusion with multispectral imagery via low-rank tensor-approximation," *IEEE Transactions on Geoscience and Remote Sensing*, vol. 59, no. 9, pp. 7817–7830, 2021.
 - [23] J. Liu, P. Musialski, P. Wonka, and J. Ye, "Tensor completion for estimating missing values in visual data," *IEEE Transactions on Pattern Analysis and Machine Intelligence*, vol. 35, no. 1, pp. 208–220, 2013.
 - [24] Y. Wang, W. Li, N. Liu, Y. Gui, and R. Tao, "Fubay: An integrated fusion framework for hyperspectral super-resolution based on bayesian tensor ring," *IEEE Transactions on Neural Networks and Learning Systems*, vol. 35, no. 10, pp. 14712–14726, 2024.
 - [25] W. Li, Y. Wang, N. Liu, C. Xiao, Z. Sun, and Q. Du, "Integrated spatio-spectral-temporal fusion via anisotropic sparsity constrained low-rank tensor approximation," *IEEE Transactions on Geoscience and Remote Sensing*, vol. 61, pp. 1–16, 2023.
 - [26] H. Xu, C. Fang, Y. Ge, Y. Gu, and J. Zheng, "Cascade-transform-based tensor nuclear norm for hyperspectral image super-resolution," *IEEE Transactions on Geoscience and Remote Sensing*, vol. 62, pp. 1–16, 2024.
 - [27] H. Xu, Y. Quan, M. Qin, Y. Wang, C. Fang, Y. Li, and J. Zheng, "Nonlinear learnable triple-domain transform tensor nuclear norm for hyperspectral image super-resolution," *IEEE Transactions on Geoscience and Remote Sensing*, vol. 63, pp. 1–17, 2025.
 - [28] L. I. Rudin, S. Osher, and E. Fatemi, "Nonlinear total variation based noise removal algorithms," *Physica D: Nonlinear Phenomena*, vol. 60, no. 1, pp. 259–268, 1992.
 - [29] Y. Yuan, Q. Wang, and X. Li, "Hyperspectral and multispectral image fusion using non-convex relaxation low rank and total variation regularization," in *IGARSS 2020 - 2020 IEEE International Geoscience and Remote Sensing Symposium*, 2020, pp. 2683–2686.
 - [30] F. Li, Y. Deng, S. Zhang, Y. Liang, H. Wang, C. Deng, and J. Li, "Multispectral and hyperspectral image fusion via joint low-rank and smooth tensor prior," in *IGARSS 2024 - 2024 IEEE International Geoscience and Remote Sensing Symposium*, 2024, pp. 9298–9301.
 - [31] Y. Chen, J. Zeng, W. He, X.-L. Zhao, and T.-Z. Huang, "Hyperspectral and multispectral image fusion using factor smoothed tensor ring decomposition," *IEEE Transactions on Geoscience and Remote Sensing*, vol. 60, pp. 1–17, 2022.
 - [32] T. Xu, T.-Z. Huang, L.-J. Deng, X.-L. Zhao, and J. Huang, "Hyperspectral image superresolution using unidirectional total variation with Tucker decomposition," *IEEE Journal of Selected Topics in Applied Earth Observations and Remote Sensing*, vol. 13, pp. 4381–4398, 2020.
 - [33] H. V. Nguyen, M. O. Ulfarsson, J. R. Sveinsson, and M. Dalla Mura, "Deep sure for unsupervised remote sensing image fusion," *IEEE Transactions on Geoscience and Remote Sensing*, vol. 60, pp. 1–13, 2022.
 - [34] M. Zhang, J. Xu, J. Zhang, H. Zhao, W. Shang, and X. Gao, "Sph-net: Hyperspectral image super-resolution via smoothed particle hydrodynamics modeling," *IEEE Transactions on Cybernetics*, vol. 54, no. 7, pp. 4150–4163, 2024.

- [35] R. Dian, A. Guo, and S. Li, “Zero-shot hyperspectral sharpening,” *IEEE Transactions on Pattern Analysis and Machine Intelligence*, vol. 45, no. 10, pp. 12 650–12 666, 2023.
- [36] Q. Ma, J. Jiang, X. Liu, and J. Ma, “Learning a 3d-cnn and transformer prior for hyperspectral image super-resolution,” *Information Fusion*, vol. 100, p. 101907, 2023.
- [37] H. Wang, J. Peng, W. Qin, J. Wang, and D. Meng, “Guaranteed tensor recovery fused low-rankness and smoothness,” *IEEE Transactions on Pattern Analysis and Machine Intelligence*, vol. 45, no. 9, pp. 10990–11 007, 2023.
- [38] L. De Lathauwer, “Decompositions of a higher-order tensor in block terms—part ii: Definitions and uniqueness,” *SIAM Journal on Matrix Analysis and Applications*, vol. 30, no. 3, pp. 1033–1066, 2008.
- [39] Z. Lin, R. Liu, and Z. Su, “Linearized alternating direction method with adaptive penalty for low-rank representation,” in *Proceedings of the 25th International Conference on Neural Information Processing Systems*, ser. NIPS’11. Red Hook, NY, USA: Curran Associates Inc., 2011, p. 612–620.
- [40] J. Yang and X. Yuan, “Linearized augmented lagrangian and alternating direction methods for nuclear norm minimization,” *Mathematics of computation*, vol. 82, no. 281, pp. 301–329, 2013.
- [41] W. Karush, “Minima of functions of several variables with inequalities as side constraints,” Master’s thesis, University of Chicago, Chicago, IL, USA, 1939.
- [42] H. W. Kuhn and A. W. Tucker, “Nonlinear programming,” in *Proceedings of the Second Berkeley Symposium on Mathematical Statistics and Probability*. Berkeley, CA, USA: University of California Press, 1951, pp. 481–492.
- [43] S. Boyd and L. Vandenberghe, *Convex Optimization*. Cambridge, UK: Cambridge University Press, 2004.
- [44] C. Lu, J. Feng, Y. Chen, W. Liu, Z. Lin, and S. Yan, “Tensor robust principal component analysis with a new tensor nuclear norm,” *IEEE Transactions on Pattern Analysis and Machine Intelligence*, vol. 42, no. 4, pp. 925–938, 2020.
- [45] H. Xu, J. Zheng, X. Yao, Y. Feng, and S. Chen, “Fast tensor nuclear norm for structured low-rank visual inpainting,” *IEEE Transactions on Circuits and Systems for Video Technology*, vol. 32, no. 2, pp. 538–552, 2022.
- [46] M. E. Kilmer and C. D. Martin, “Factorization strategies for third-order tensors,” *Linear Algebra and its Applications*, vol. 435, no. 3, pp. 641–658, 2011, special Issue: Dedication to Pete Stewart on the occasion of his 70th birthday.
- [47] H. Wang, F. Zhang, J. Wang, T. Huang, J. Huang, and X. Liu, “Generalized nonconvex approach for low-tubal-rank tensor recovery,” *IEEE Transactions on Neural Networks and Learning Systems*, vol. 33, no. 8, pp. 3305–3319, 2022.
- [48] Y. Wang, W. Li, Y. Gui, Q. Du, and J. E. Fowler, “A generalized tensor formulation for hyperspectral image super-resolution under general spatial blurring,” *IEEE Transactions on Pattern Analysis and Machine Intelligence*, pp. 1–15, 2025.
- [49] Y. Wang, W. Li, Y. Gui, H. Xie, and L. Zhang, “A generalized non-convex surrogated framework for anomaly detection on blurred hyperspectral images,” *IEEE Transactions on Image Processing*, pp. 1–1, 2025.
- [50] J. H. Friedman, “Fast sparse regression and classification,” *International Journal of Forecasting*, vol. 28, no. 3, pp. 722–738, 2012.
- [51] J. Wright and Y. Ma, *High-Dimensional Data Analysis with Low-Dimensional Models: Principles, Computation, and Applications*. Cambridge University Press, 2022.
- [52] X. Zhang, J. Zheng, D. Wang, G. Tang, Z. Zhou, and Z. Lin, “Structured sparsity optimization with non-convex surrogates of $\ell_{2,0}$ -norm: A unified algorithmic framework,” *IEEE Transactions on Pattern Analysis and Machine Intelligence*, vol. 45, no. 5, pp. 6386–6402, 2023.
- [53] B. Wang, X. Xiong, Y. Lian, X. Cao, H. Zhou, K. Yu, and Z. Liu, “Perceptive spectral transformer unfolding network with multiscale mixed training for arbitrary-scale hyperspectral and multispectral image fusion,” *Information Fusion*, vol. 122, p. 103166, 2025.